Analysis of the optical spectra and paramagnetic susceptibility of DyOF

1996 J. Phys.: Condens. Matter 8 1575

(http://iopscience.iop.org/0953-8984/8/10/027)

J. Phys.: Condens. Matter **8** (1996) 1575–1590. Printed in the UK

Analysis of the optical spectra and paramagnetic susceptibility of DyOF

Jorma Hölsä†, Eija Kestilä†¶, Pia Ylhä†, Regino Sáez-Puche‡, Przemyslaw Dereń§, Wiesław Stręk§ and Pierre Porcher‖

† University of Turku, Department of Chemistry, FIN-20014 Turku, Finland
‡ Universidad Complutense de Madrid, Facultad de Ciencias Químicas, Departamento de Química Inorgánica I, E-28040 Madrid, Spain
§ Polish Academy of Sciences, W Trzebiatowski Institute of Low-Temperature and Structure Research, PL-50 950 Wrocław, Poland
‖ CNRS, UPR 209, F-92195 Meudon, France

Received 22 August 1995, in final form 27 November 1995

Abstract. The optical absorption spectra of the rhombohedral DyOF were measured at selected temperatures between 9 and 300 K. The emission spectra of the Dy^{3+} ion in the LaOF and GdOF matrices were obtained at 77 K and room temperature. The energy level scheme of Dy^{3+} ($4f^9$ electron configuration) was simulated with a Hamiltonian of 20 parameters. The diagonalization of the energy matrices including simultaneously the free ion and crystal field (c.f.) interactions was carried out for the C_{3v} point symmetry of the RE^{3+} site. Good correlation with an rms deviation of 17 cm^{-1} was obtained between the experimental and calculated energy level schemes of 153 Kramers doublets. The c.f. parameters show only slight distortion from O_h symmetry. A comparison to Pr^{3+} ($4f^2$), Nd^{3+} ($4f^3$), Sm^{3+} ($4f^5$), Eu^{3+} ($4f^6$), and Tb^{3+} ($4f^8$ electron configuration) in other REOF matrices showed smooth evolution of the c.f. effect which was discussed in terms of the possible interactions involved. The x-ray powder diffraction pattern of DyOF between $6.5^\circ < 2\theta < 120^\circ$ was analysed by the Rietveld profile refinement method. The structural data were used to calculate the c.f. parameters by the modified electrostatic point charge model yielding B_0^4, B_3^4 and B_0^6 values close to the experimental ones, whereas the B_0^2, B_3^6, and B_6^6 values were too large. Using the experimental free ion and c.f. wave functions, the paramagnetic susceptibility of DyOF as a function of temperature was simulated. Above the Néel temperature (3.6 K), good agreement was obtained between the calculated and experimental susceptibilities in the paramagnetic range.

1. Introduction

The bulk of our knowledge of the electronic level structure of the rare earth (RE) ions ($4f^N$ electron configurations) has been obtained by optical spectroscopy. Even in the solid state, the 4f electrons of the RE^{3+} ions are well protected from the ligand interaction and, consequently, they interact only weakly with the electrons of neighbouring atoms giving spectral and other physical properties characteristic of the particular RE^{3+} ion.

The Dy^{3+} ion has a $4f^9$ electron configuration which results in one of the most complicated energy level schemes among all RE^{3+} ions. The $4f^9$ configuration is characterized by 198 *SLJ* manifolds which split in the presence of the crystal field (c.f.) interaction into a total of 1001 sublevels (Stark levels). The low-lying ^6H and ^6F multiplets

¶ Author to whom all correspondence should be addressed.

0953-8984/96/101575+16$19.50

form rather isolated groups up to $\sim$20 000 cm^{-1} [1] above which the density of the states becomes high and the mixing of states with the same and different J value increases. Because of the difficult interpretation of the optical spectra, only a few detailed spectroscopic studies concerning the Dy^{3+} ion in inorganic matrices have been carried out so far. The energy level scheme of Dy^{3+} has been analysed by using a phenomenological model including separately the free ion and c.f. effects for the simple fluoride LaF_3:Dy^{3+} [1–3], and chloride $LaCl_3$:Dy^{3+} [4, 5] systems. Some c.f. calculations using a small basic set of c.f. levels have been performed for Y_2O_3:Dy^{3+} [6, 7], $YAlO_3$:Dy^{3+} [8], $Dy_2Ge_2O_7$ [9], elpasolites [10], $LiYF_4$:Dy^{3+} [11], $CaWO_4$:Dy^{3+} [12], CaS:Dy^{3+} [13], and $Dy_3Ga_5O_{12}$ [14].

The rare earth oxyhalides, REOX (X = F, Cl, Br, and I), offer a versatile system where an interchange of both the cation and anion leads to interesting structural modifications. This series provides an opportunity for a systematic study of the c.f. effect in both the RE and halide series, too. The stoichiometric RE oxyfluorides, REOF (RE = La–Lu and Y) [15–17] have trigonal symmetry due to the three-dimensionally linked ORE_4 units [16]. The heavier REOF (RE = Tm, Yb, and Lu) seem to have also a monoclinic structure [18]. The nonstoichiometric oxyfluorides, $REO_{1-x}F_{1+2x}$, for example $LaO_{0.65}F_{1.70}$ [19], have (distorted) tetragonal symmetry due to the two-dimensional network of the ORE_4 units.

In this work, the structure of the stoichiometric hexagonal DyOF was refined from x-ray powder diffraction data by using the Rietveld method. With those results, the c.f. parameters were calculated by using a modified electrostatic point charge model (PCEM). The energy level scheme of the Dy^{3+} ion in DyOF was also deduced from the optical absorption and luminescence spectra. The experimental energy level scheme was simulated with a phenomenological model using 14 free ion parameters describing the electrostatic and interconfigurational interactions as well as the spin–orbit coupling. The c.f. effect was simultaneously taken into account by six B_q^k parameters. The phenomenological c.f. parameters were compared to those obtained from the PCEM calculations. From the c.f. parameter values the extent of the distortion from the ideal cubic fluorite-type structure was deduced. The evolution of the c.f. effect in the REOF:RE^{3+} series (RE^{3+} = Pr^{3+}, Nd^{3+}, Sm^{3+}, Eu^{3+}, Tb^{3+}, and Dy^{3+}) [20–24] was analysed in terms of the interactions possibly involved. The paramagnetic susceptibility of DyOF as a function of temperature was calculated using the wave functions obtained from the energy level simulation and was compared to the experimental values.

2. Experimental details

2.1. Sample preparation

The polycrystalline REOF samples were prepared by the solid state reaction between RE_2O_3 and NH_4F [25]. An excess of NH_4F (NH_4F/Dy_2O_3 ratio = 4.5) was utilized while heating the reactants at 860 °C for 1.5 h in order to obtain the stoichiometric DyOF. For the luminescence measurements, the LaOF and GdOF hosts were doped with 1 mol% of Dy^{3+}. The reaction temperature was 1050 and 950 °C for LaOF and GdOF, respectively, and a stoichiometric NH_4F/RE_2O_3 ratio (= 2.00) was used. All samples were confirmed by routine x-ray powder diffraction to be of the correct stoichiometric REOF form. No presence of the nonstoichiometric phase of excess fluoride could be observed. The absence of additional lines in the optical spectra indicated that no additional phases were present.

2.2. X-ray powder diffraction measurements

The diffraction data of pure DyOF were collected at room temperature with an Enraf-Nonius PDS120 x-ray powder diffractometer using an INEL position sensitive detector. The XRD patterns for structure refinement were measured in the 2θ region between 6.5 and 120°. The monochromatic Cu K_{α_1} line ($\lambda = 1.540\,598$ Å) was used as a radiation source.

2.3. Optical measurements

The luminescence spectra of the Dy^{3+} doped LaOF and GdOF were recorded at 77 and 300 K in the visible region between 500 and 800 nm. The luminescence was excited with the Ar^+ lines at 457.9 and 488.0 nm of a Carl Zeiss Jena ILA 120-1 laser, dispersed by a 1 m Czerny–Tuner type Jobin Yvon monochromator and detected by Hamamatsu R950 and R406 photomultipliers equipped with standard electronics. The resolution of the equipment was around 1 cm^{-1}.

The optical absorption spectra of the pure hexagonal DyOF between 280 and 1700 nm were measured at selected temperatures between 9 and 300 K by a Cary 5E UV–vis–NIR spectrophotometer. The instrument was equipped with auto-calibration of the wavelength scale which resulted in reproducibility of the measurements better than 2 Å. The band width of 0.6 Å used in measurements was sufficient taking into account the width of the absorption lines. The samples were prepared by adding 10 to 15 mass % of DyOF to KBr and pressing a transparent disc of a thickness of 1 mm.

2.4. Magnetic measurements

The magnetic susceptibility measurements were carried out using a Quantum Design SQUID magnetometer. The available temperature range was from 1.7 to 400 K and the magnetic field used was 1000 Oe. The apparatus was calibrated using metallic Pd and $Hg[Co(SCN)_4]$ as standards. The molar magnetic susceptibility of DyOF was corrected for the ionic diamagnetism with the values -12×10^{-6}, -11×10^{-6}, and -19×10^{-6} emu mol^{-1} for O^{2-}, F^-, and Dy^{3+}, respectively [26].

3. Results and discussion

3.1. Crystal structure

The powder XRD data for DyOF were analysed with the Rietveld profile refinement method using the program DBSW-9006PC [27]. The unit cell, atomic positional parameters, thermal factors, and profile coefficients were all refined. The Gaussian peak shape modified for peak asymmetry was applied to the data in the $17° \leqslant 2\theta \leqslant 120°$ range. The refined unit cell and atomic positional parameters for YOF [17] were used as starting values for the refinement. The refinement was carried out to a constant value (5.5%) of the weighted pattern R-factor, R_{wp}.

The structure of the stoichiometric DyOF belongs to the hexagonal (or rhombohedral) crystal system with $R\bar{3}m$—D_{3d}^5 (No 166 in [28]; $Z = 6$) as the space group. The hexagonal unit cell dimensions found in our calculations are $a = 3.7954(1)$ and $c = 18.8892(2)$ Å. All atoms lie in a special position with $x = y = 0$ while the z coordinates are as follows: $z_{RE} = 0.241\,44(2)$, $z_O = 0.119\,46(10)$, and $z_F = 0.368\,77(2)$. The positional parameter values are close to those for the ideal cubic structure, $z_{RE} = 0.250$, $z_O = 0.125$, and $z_F = 0.375$ [17].

The coordination polyhedron around the RE atom is a bicapped trigonal antiprism with the RE–F distances ($1 \times 2.405(20)$ and $3 \times 2.437(2)$ Å) longer than the RE–O distances ($1 \times 2.304(21)$ and $3 \times 2.252(5)$ Å). The distance from the RE atom to the capping oxygen along the threefold axis is longer than the others while the situation is reversed for the RE–F distances. The RE atom resides in a site with C_{3v} point symmetry. The four different Dy–O(F)–Dy angles are between 102 and 116°.

3.2. Analysis of the optical spectra

3.2.1. Selection rules. The electronic transitions between the free ion levels of Dy^{3+} are induced either by the electric (e.d.) or magnetic dipole (m.d.) interactions and have thus multipolar character. The bulk of the transitions originates from the e.d. interactions according to the $\Delta J \leqslant 6$ selection rule but the probability of observing the m.d. transitions with the selection rule $\Delta J = 0, \pm 1$ is non-negligible [29].

For the Kramers ions such as Dy^{3+}, the number of the Stark levels for a particular free ion $^{2S+1}L_J$ state is $J + 1/2$ for any symmetry lower than cubic. This gives rise to a total of 1001 levels for the $4f^9$ configuration [30]. For the C_{3v} site symmetry, the Dy^{3+} ion has only two types of Stark level corresponding to the irreducible representation $D_{1/2}$ and the Kramers conjugate level (S_1, S_3). According to the group theoretical selection rules, the transitions between all c.f. levels are allowed as both the e.d. and m.d. transitions [30].

3.2.2. Luminescence spectra. The visible emission of the Dy^{3+} ion originating from the $^4F_{9/2}$ state to $^6H_{13/2}$ and $^6H_{11/2}$ was recorded for the LaOF and GdOF matrices. The emission to the $^6H_{15/2}$ ground state could not be observed because the $^4F_{9/2} \rightarrow {}^6H_{15/2}$ transition energy was too close to the Ar^+ excitation line at 457.9 nm. Not all components of the $^6H_{13/2}$ and $^6H_{11/2}$ states were observed since only five and four out of seven and six, respectively, were found in the GdOF matrix (table 1). The data for the LaOF matrix were even sparser. The energy levels observed in the GdOF matrix were used in the calculations to minimize the effect of the ionic radius difference between the Dy^{3+} ion and the host cation.

The c.f. splitting of the $^6H_{11/2}$ state was observed from both the luminescence and absorption measurements. The DyOF matrix was used for the absorption measurements and thus the environment of the Dy^{3+} ion is different from the LaOF and GdOF matrices. Due to the difference in the ionic radius between the La^{3+} or Gd^{3+} and the Dy^{3+} ion, the energies and splitting of the $^6H_{11/2}$ Stark levels were not exactly the same. The maximum deviation of the Stark-level energies observed in the luminescence and absorption measurements was about 20 cm^{-1} because of the different matrices.

3.2.3. Absorption spectra. The optical absorption of Dy^{3+} in DyOF was measured at selected temperatures between 9 and 300 K in order to find out the splitting of the $^6H_{15/2}$ ground state inaccessible by the luminescence measurements. From the hot band absorption, the energies of the six lowest Stark levels of the ground state (0, 12, 57, 72, 134, and 449 cm^{-1}) were confirmed.

In the NIR area, 31 Stark levels out of the theoretical 39 for the $^6H_{11/2-5/2}$ and $^6F_{11/2-1/2}$ states were observed (figures 1 and 2). Five Stark levels out of six were observed for the first excited state $^6H_{11/2}$ from absorption spectra between 1700 and 1650 nm. The absorption to the $^6H_{9/2}$ and $^6F_{11/2}$ as well as to the $^6H_{7/2}$ and $^6F_{9/2}$ states partially overlaps in the energy region from 1220 to 1333 and 1043 to 1120 nm, respectively. The region containing the $^6H_{9/2}$ and $^6F_{11/2}$ states was characterized by two large combination lines which are

Table 1. The observed and calculated energy levels of DyOF in cm^{-1} units.

The main component		E_{obs}	E_{calc}	The main component		E_{obs}	E_{calc}
$^6H_{15/2}$ 1/2	$D_{1/2}$	0.1	−5	$^6F_{5/2}$ 1/2	$D_{1/2}$	12 613	12 604
15/2	(S_1, S_3)	12	3	$^6F_{3/2}$ 3/2	(S_1, S_3)	13 287	13 296
13/2	$D_{1/2}$	57	64	1/2	$D_{1/2}$	13 309	13 304
3/2	(S_1, S_3)	72	67	$^6F_{1/2}$ 1/2	$D_{1/2}$	13 832	13 837
−5/2	$D_{1/2}$	134	130	$^4F3_{9/2}$ 9/2	(S_1, S_3)	20 862	20 881
−11/2	$D_{1/2}$	446	424	1/2	$D_{1/2}$		20 911
7/2	$D_{1/2}$		485	3/2	(S_1, S_3)	21 052	21 044
9/2	(S_1, S_3)		492	−5/2	$D_{1/2}$	21 084	21 072
$^6H_{13/2}$ 13/2	$D_{1/2}$	3526	3531	7/2	$D_{1/2}$	21 505	21 490
−5/2	$D_{1/2}$	3547	3570	$^4I3_{15/2}$ 15/2	(S_1, S_3)		21 816
3/2	(S_1, S_3)	3568	3581	1/2	$D_{1/2}$	21 934	21 907
7/2	$D_{1/2}$		3587	3/2	(S_1, S_3)	21 953	21 981
1/2	$D_{1/2}$	3685	3711	−5/2	$D_{1/2}$	22 044	22 008
−11/2	$D_{1/2}$	3743	3750	1/2	$D_{1/2}$	22 261	22 250
9/2	(S_1, S_3)		3766	−9/2	(S_1, S_3)		22 290
$^6H_{11/2}$ −5/2	$D_{1/2}$		5896	13/2	$D_{1/2}$		22 304
9/2	(S_1, S_3)	5929	5921	11/2	$D_{1/2}$	22 320	22 315
7/2	$D_{1/2}$	5943	5927	$^4G4_{11/2}$ 9/2	(S_1, S_3)		23 334
3/2	(S_1, S_3)	5959	5973	7/2	$D_{1/2}$	23 379	23 343
−11/2	$D_{1/2}$	5977	5980	−5/2	$D_{1/2}$	23 390	23 366
1/2	$D_{1/2}$	5998	6008	3/2	(S_1, S_3)	23 459	23 478
$^6H_{9/2}$ −5/2	$D_{1/2}$	7571	7571	−11/2	$D_{1/2}$	23 472	23 487
9/2	(S_1, S_3)	7622	7586	1/2	$D_{1/2}$	23 535	23 572
$^6F_{11/2}$ 1/2	$D_{1/2}$	7643	7666	$^4M_{21/2}$ 21/2	(S_1, S_3)	24 730	24 725
3/2	(S_1, S_3)	7684	7672	1/2	$D_{1/2}$	24 793	24 787
−11/2	$D_{1/2}$	7712	7698	3/2	(S_1, S_3)	24 810	24 820
−5/2	$D_{1/2}$		7826	−5/2	$D_{1/2}$	24 831	24 843
$^6H_{9/2}$ 3/2	(S_1, S_3)	7855	7851	1/2	$D_{1/2}$	24 970	24 994
$^6F_{11/2}$ −5/2	$D_{1/2}$	7870	7860	3/2	(S_1, S_3)	25 106	25 107
$^6H_{9/2}$ 1/2	$D_{1/2}$	7890	7895	19/2	$D_{1/2}$	25 118	25 125
$^6F_{11/2}$ 7/2	$D_{1/2}$		8113	−17/2	$D_{1/2}$		25 166
9/2	(S_1, S_3)	8164	8167	13/2	$D_{1/2}$	25 307	25 305
$^6F_{9/2}$ −5/2	$D_{1/2}$		8931	−11/2	$D_{1/2}$		25 330
$^6H_{7/2}$ 3/2	(S_1, S_3)	8988	8982	15/2	(S_1, S_3)		25 331
$^6F_{9/2}$ 7/2	$D_{1/2}$	9008	8993	13/2	$D_{1/2}$	25 362	25 347
1/2	$D_{1/2}$		9219	$^4I3_{13/2}$ 13/2	$D_{1/2}$		25 406
3/2	(S_1, S_3)	9240	9220	3/2	(S_1, S_3)	25 435	25 427
$^6H_{7/2}$ 1/2	$D_{1/2}$	9252	9260	1/2	$D_{1/2}$	25 449	25 436
$^6F_{9/2}$ 9/2	(S_1, S_3)		9265	$^4K1_{17/2}$ 1/2	$D_{1/2}$	25 626	25 618
$^6H_{7/2}$ 7/2	$D_{1/2}$	9295	9317	9/2	(S_1, S_3)		25 653
−5/2	$D_{1/2}$	9575	9588	7/2	$D_{1/2}$		25 653
$^6H_{5/2}$ 1/2	$D_{1/2}$		10 193	−17/2	$D_{1/2}$	25 687	25 688
−5/2	$D_{1/2}$		10 303	−11/2	$D_{1/2}$	25 731	25 780
3/2	(S_1, S_3)	10 348	10 335	$^4F3_{7/2}$ 1/2	$D_{1/2}$	25 835	25 822
$^6F_{7/2}$ −5/2	$D_{1/2}$	10 995	11 004	$^4K1_{17/2}$ 9/2	(S_1, S_3)	25 843	25 842
1/2	$D_{1/2}$	11 170	11 177	1/2	$D_{1/2}$	25 860	25 880
7/2	$D_{1/2}$	11 211	11 209	$^4F3_{7/2}$ 3/2	(S_1, S_3)	25 878	25 891
3/2	(S_1, S_3)	11 220	11 220	$^4K1_{17/2}$ −5/2	$D_{1/2}$	25 917	25 915
$^6F_{5/2}$ 3/2	(S_1, S_3)	12 446	12 457	$^4I3_{13/2}$ 1/2	$D_{1/2}$	25 931	25 955
−5/2	$D_{1/2}$	12 456	12 473	3/2	(S_1, S_3)		25 956

Table 1. (Continued)

The main component		E_{obs}	E_{calc}	The main component		E_{obs}	E_{calc}
$^4I3_{13/2\ 7/2}$	$D_{1/2}$	25 977	25 986	$^4M_{17/2\ -17/2}$	$D_{1/2}$	29 891	29 902
$^4K1_{17/2\ 13/2}$	$D_{1/2}$	25 989	26 001	$_{1/2}$	$D_{1/2}$	29 926	29 916
$^4I3_{13/2\ 9/2}$	(S_1, S_3)		26 010	$_{-11/2}$	$D_{1/2}$	29 961	29 951
$_{-11/2}$	$D_{1/2}$	26 033	26 036	$_{13/2}$	$D_{1/2}$	29 976	29 965
$^4M_{19/2\ 19/2}$	$D_{1/2}$		26 073	$_{15/2}$	(S_1, S_3)	29 996	29 967
$_{9/2}$	(S_1, S_3)		26 107	$^4G4_{9/2\ 1/2}$	$D_{1/2}$		30 168
$_{-5/2}$	$D_{1/2}$		26 109	$_{3/2}$	(S_1, S_3)		30 181
$_{7/2}$	$D_{1/2}$	26 162	26 133	$^4M_{17/2\ 13/2}$	$D_{1/2}$		30 242
$_{13/2}$	$D_{1/2}$	26 308	26 315	$_{-11/2}$	$D_{1/2}$		30 304
$_{3/2}$	(S_1, S_3)	26 376	26 383	$_{9/2}$	(S_1, S_3)	30 343	30 314
$_{13/2}$	$D_{1/2}$		26 388	$^6P_{3/2\ 1/2}$	$D_{1/2}$		30 754
$_{1/2}$	$D_{1/2}$		26 411	$_{3/2}$	(S_1, S_3)	30 777	30 765
$_{-17/2}$	$D_{1/2}$	26 442	26 434	$^4K1_{15/2\ 1/2}$	$D_{1/2}$	30 817	30 819
$_{15/2}$	(S_1, S_3)	26 503	26 463	$_{13/2}$	$D_{1/2}$	30 900	30 904
$^4P2_{3/2\ 1/2}$	$D_{1/2}$	27 316	27 311	$_{3/2}$	(S_1, S_3)	30 918	30 910
$_{3/2}$	(S_1, S_3)	27 333	27 333	$_{11/2}$	$D_{1/2}$	30 983	30 976
$^6P_{5/2\ -5/2}$	$D_{1/2}$	27 380	27 381	$_{15/2}$	(S_1, S_3)	31 007	30 981
$_{3/2}$	(S_1, S_3)	27 385	27 383	$_{-5/2}$	$D_{1/2}$	31 035	31 032
$_{1/2}$	$D_{1/2}$	27 395	27 405	$_{7/2}$	$D_{1/2}$		31 224
$^4I3_{11/2\ -11/2}$	$D_{1/2}$		27 723	$_{9/2}$	(S_1, S_3)	31 235	31 240
$_{1/2}$	$D_{1/2}$	27 785	27 810	$^4L_{19/2\ 7/2}$	$D_{1/2}$	31 256	31 261
$_{3/2}$	(S_1, S_3)	27 797	27 812	$_{-17/2}$	$D_{1/2}$	31 272	31 283
$_{-5/2}$	$D_{1/2}$	27 856	27 856	$_{3/2}$	(S_1, S_3)	31 284	31 311
$_{9/2}$	(S_1, S_3)		28 010	$_{7/2}$	$D_{1/2}$		31 314
$_{7/2}$	$D_{1/2}$	28 036	28 016	$_{-11/2}$	$D_{1/2}$		31 351
$^4M_{15/2\ 15/2}$	(S_1, S_3)		28 172	$_{7/2}$	$D_{1/2}$		31 359
$_{7/2}$	$D_{1/2}$		28 232	$_{15/2}$	(S_1, S_3)	31 392	31 386
$_{-5/2}$	$D_{1/2}$		28 236	$_{1/2}$	$D_{1/2}$	31 420	31 423
$_{3/2}$	(S_1, S_3)		28 249	$_{9/2}$	(S_1, S_3)		31 454
$^6P_{7/2\ 3/2}$	(S_1, S_3)	28 390	28 390	$_{13/2}$	$D_{1/2}$	31 482	31 462
$_{1/2}$	$D_{1/2}$		28 391	$^4K1_{15/2\ -11/2}$	$D_{1/2}$	31 521	31 544
$_{-5/2}$	$D_{1/2}$	28 407	28 404	$_{9/2}$	(S_1, S_3)		31 594
$_{7/2}$	$D_{1/2}$	28 432	28 432	$_{7/2}$	$D_{1/2}$		31 620
$^4M_{15/2\ 1/2}$	$D_{1/2}$	28 628	28 616	$^4G2_{7/2\ 7/2}$	$D_{1/2}$		31 714
$_{9/2}$	(S_1, S_3)	28 643	28 631	$^4D2_{5/2\ 1/2}$	$D_{1/2}$		31 867
$_{13/2}$	$D_{1/2}$	28 657	28 674	$^4P2_{1/2\ 1/2}$	$D_{1/2}$		32 013
$_{-11/2}$	$D_{1/2}$	28 725	28 741	$^4D2_{5/2\ 5/2}$	$D_{1/2}$		32 039
$^4I3_{9/2\ 9/2}$	(S_1, S_3)		29 336	$_{3/2}$	(S_1, S_3)		32 095
$_{1/2}$	$D_{1/2}$		29 373	$^4H1_{13/2\ 7/2}$	$D_{1/2}$	32 956	32 987
$_{9/2}$	(S_1, S_3)		29 493	$_{-11/2}$	$D_{1/2}$	33 021	33 038
$_{-5/2}$	$D_{1/2}$	29 510	29 496	$_{13/2}$	$D_{1/2}$	33 042	33 040
$^4G4_{9/2\ 7/2}$	$D_{1/2}$	29 640	29 635	$_{9/2}$	(S_1, S_3)	33 052	33 041
$^4F3_{5/2\ 1/2}$	$D_{1/2}$	29 655	29 659	$^4K1_{13/2\ 1/2}$	$D_{1/2}$	33 063	33 069
$^4I3_{9/2\ 3/2}$	(S_1, S_3)		29 811	$^4H1_{13/2\ 9/2}$	(S_1, S_3)	33 083	33 079
$^4M_{17/2\ -5/2}$	$D_{1/2}$		29 816	$^4K1_{13/2\ -11/2}$	$D_{1/2}$	33 100	33 083
$^4I3_{9/2\ 7/2}$	$D_{1/2}$		29 825	$^4H1_{13/2\ -11/2}$	$D_{1/2}$	33 329	33 333
$^4M_{17/2\ 3/2}$	(S_1, S_3)	29 847	29 842	$_{9/2}$	(S_1, S_3)	33 346	33 334
$^4I3_{9/2\ -5/2}$	$D_{1/2}$	29 865	29 870	$^4K1_{13/2\ 9/2}$	(S_1, S_3)	33 350	33 352
$^4M_{17/2\ 9/2}$	(S_1, S_3)	29 875	29 888	$^4H1_{13/2\ 13/2}$	$D_{1/2}$	33 376	33 365

Table 1. (Continued)

The main component		E_{obs}	E_{calc}	The main component		E_{obs}	E_{calc}
$^4H1_{13/2}$ 13/2	$D_{1/2}$	33 401	33 409	$^4L_{17/2}$ −5/2	$D_{1/2}$		34 301
1/2	$D_{1/2}$		33 419	3/2	(S_1, S_3)		34 345
$^4L_{13/2}$ 7/2	$D_{1/2}$	33 479	33 449	17/2	$D_{1/2}$	34 349	34 348
$^4F3_{3/2}$ 1/2	$D_{1/2}$	33 519	33 522	1/2	$D_{1/2}$		34 368
3/2	(S_1, S_3)		33 526	9/2	(S_1, S_3)	34 379	34 378
$^4H1_{11/2}$ 1/2	$D_{1/2}$		33 823	7/2	$D_{1/2}$		34 396
−5/2	$D_{1/2}$	33 843	33 842	7/2	$D_{1/2}$		34 403
$^4D3_{7/2}$ 3/2	(S_1, S_3)	33 853	33 846	$^4F3_{5/2}$ 1/2	$D_{1/2}$		34 524
7/2	$D_{1/2}$	33 863	33 858	$^4G2_{11/2}$ 7/2	$D_{1/2}$	34 679	34 683
$^4H1_{11/2}$ 9/2	(S_1, S_3)		33 938	9/2	(S_1, S_3)		34 683
1/2	$D_{1/2}$		33 948	5/2	$D_{1/2}$	34 719	34 724
−5/2	$D_{1/2}$	34 013	34 031	3/2	(S_1, S_3)		34 836
7/2	$D_{1/2}$		34 077	11/2	$D_{1/2}$	34 863	34 854
$^4H3_{11/2}$ 3/2	(S_1, S_3)		34 090	11/2	$D_{1/2}$		34 925
$^4H1_{11/2}$ 3/2	(S_1, S_3)		34 105	$^4K1_{11/2}$ 1/2	$D_{1/2}$		35 632
7/2	$D_{1/2}$		34 112	9/2	(S_1, S_3)		35 657
$^4G1_{9/2}$ 1/2	$D_{1/2}$		34 125	−11/2	$D_{1/2}$		35 729
$^4H1_{11/2}$ 9/2	(S_1, S_3)		34 152	−11/2	$D_{1/2}$		35 753
1/2	$D_{1/2}$		34 157	$^4H1_{7/2}$ 3/2	(S_1, S_3)		35 755
5/2	$D_{1/2}$	34 204	34 201	$^4K1_{11/2}$ 1/2	$D_{1/2}$		35 772
$^4L_{17/2}$ 15/2	(S_1, S_3)	34 223	34 223	3/2	(S_1, S_3)		35 891
1/2	$D_{1/2}$	34 272	34 253	7/2	$D_{1/2}$		35 915
15/2	(S_1, S_3)		34 291	7/2	$D_{1/2}$		35 951
13/2	$D_{1/2}$		34 301	−5/2	$D_{1/2}$		36 045

due to the overlap of three Stark levels. Absorption to nine of the 11 Stark levels of the $^6H_{9/2}$ and $^6F_{11/2}$ states was observed. The $^6H_{15/2} \rightarrow {}^6F_{11/2}$ transition is a hypersensitive transition with intensity particularly sensitive to the host material [31, 32]. The intensity of this transition is lower for DyOCl [33] than for DyOF when compared to the intensities of the other transitions. The $^6H_{15/2} \rightarrow {}^6H_{7/2}$ and $^6H_{15/2} \rightarrow {}^6F_{9/2}$ transitions have low intensity when compared to the $^6H_{15/2} \rightarrow {}^6F_{11/2}$ transition. From the $^6H_{15/2} \rightarrow {}^6H_{7/2}$, $^6F_{9/2}$ transitions six out of a theoretical nine Stark levels were observed.

The intensities of the $^6H_{15/2} \rightarrow {}^6H_{5/2}$ and $^6H_{15/2} \rightarrow {}^6F_{1/2}$ transitions were low. The transition to the $^6F_{1/2}$ state is forbidden due to the $\Delta J \leqslant 6$ free ion selection rule [29] but was observed anyhow owing to the breakdown of these selection rules by the c.f. effect. The poor quality of the spectra in the region between 800 and 950 nm (the $^6H_{15/2} \rightarrow {}^6F_{7/2}$ transition) was due to the detector change.

In the visible and UV regions, the density of the absorption lines increases (figure 3). The $^6H_{15/2} \rightarrow {}^4I3_{15/2}$ and $^6H_{15/2} \rightarrow {}^4G4_{15/2}$ transitions at wavelengths from 448 to 458 and 424 to 428 nm, respectively, yielded the last well resolved lines, beyond which the J mixing of states becomes high. The transition of high intensity at 352 nm was assigned to $^6H_{15/2} \rightarrow {}^6P_{7/2}$. The last Stark levels, attributed to the absorption to the $^4G2_{11/2}$ state, were observed at 287 nm. The transitions to the higher levels of the $4f^9$ configuration were hidden by a large band absorption due to the activator–host lattice interaction. Most of the levels of the $4f^9$ configuration are thus inaccessible with one-photon absorption techniques.

The lines marked with an asterisk in the absorption spectra are associated with transitions which originate from the coupling between the pure electronic zero-phonon lines and lattice vibrations [34]. The coupling is most clearly seen in the NIR region (figures 1 and 2). The

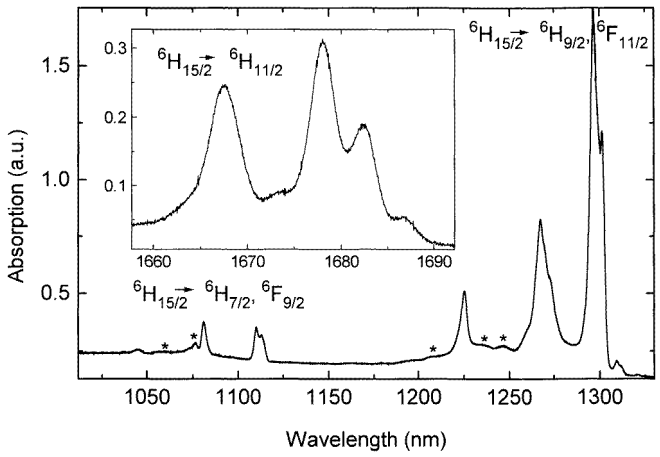

Figure 1. The NIR absorption spectra of DyOF at 10 K at wavelengths between 1000 and 1700 nm. The vibronic transitions are marked with an asterisk.

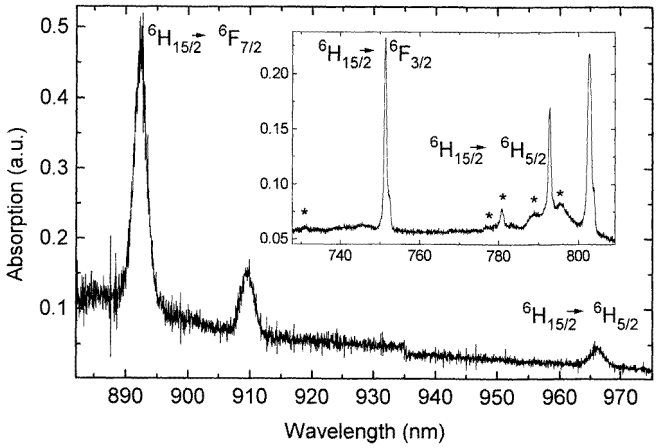

Figure 2. The NIR absorption spectra of DyOF at 10 K at wavelengths between 720 and 975 nm. The vibronic transitions are marked with an asterisk.

vibronic lines could be confirmed by the Raman and IR spectra of the REOF series [35]. Lines corresponding to frequencies 250 and 360 cm^{-1} were usually found. Moreover, the analysis of the line shapes and the line intensities as a function of the temperature excluded the vibronic lines with high probability.

The number of the Stark levels observed from absorption spectra was 149 which represents 39 *SLJ* manifolds including the $^6H_{15/2}$ ground state as well as $^6H_{11/5-5/2}$, $^6F_{11/2-1/2}$, $^4F3_{9/2-3/2}$, $^4I3_{15/2-9/2}$, $^4G4_{11/2-7/2}$, $^4M2_{1/2-17/2}$, $^4K1_{17/2,11/2}$, $^6P3_{7/2-3/2}$, $^4D2_{5/2}$, $^4P2_{3/2}$, $^4L_{13/2,11/2}$, $^4H1_{13/2-11/2}$, $^4D3_{11/2}$, $^4G1_{11/2}$, and $^4G2_{11/2}$ (table 1).

3.3. Simulation of the energy level scheme

3.3.1. Theoretical treatment of experimental data. The most important interactions describing the free ion energy level structure of the RE^{3+} ions are the Coulombic and

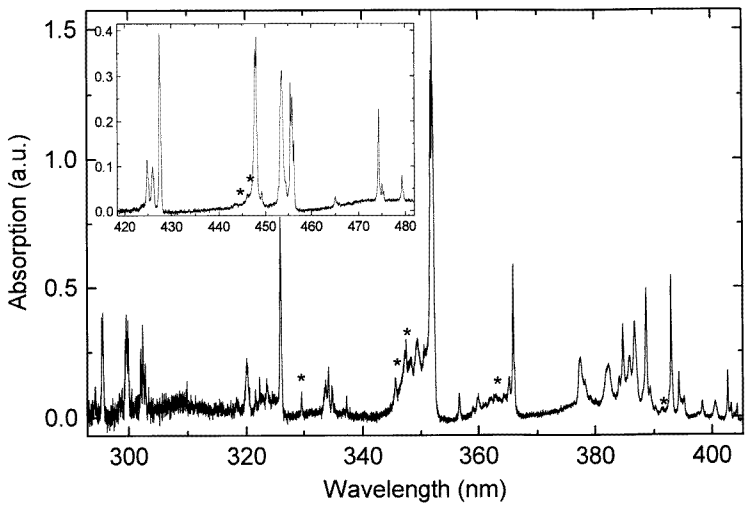

Figure 3. The UV and visible absorption spectra of DyOF at 10 K at wavelengths between 275 and 485 nm. The vibronic transitions are marked with an asterisk.

spin–orbit interactions. When only these interactions are used, however, discrepancies of an order of a few hundred wave numbers remain between the calculated and experimental energy levels [36]. Minor contributions include the spin-independent two- and three-body interactions between the 4f and different excited configurations as well as the c.f. effect. The corresponding effective Hamiltonian H can then be described as follows [29]:

$$H = H_0 - \sum_{k=0,1,2,3} E_k(n\mathrm{f}, n\mathrm{f})\,\mathrm{e}^k + \zeta_{4f} A_{\mathrm{SO}} + \alpha L(L+1) + \beta G(\mathrm{G}_2) + \gamma \mathrm{G}(\mathrm{R}_7) + \sum_{k=2,3,4,6,7,8} T^k t_k + \sum_{k,q,i} B_q^k C_q^k(i) \tag{1}$$

where H_0 is the one-electron part of the free ion Hamiltonian where the potential seen by an electron on a rare earth ion is treated as spherically symmetric. E_k (Racah parameters) and $\zeta_{4\mathrm{f}}$ are the electrostatic and spin–orbit integrals whereas e^k and A_{SO} represent the angular parts of these interactions, respectively. Spin-independent configuration interaction arises from coupling of configurations by the Coulomb interaction and can be described by the two- and three-body terms. The former include the Trees parameters α, β, and γ with L as the total orbital angular momentum of the levels involved. $G(\mathrm{G}_2)$ and $G(\mathrm{R}_7)$ are the Casimir operators for the Lie groups G_2 and R_7, respectively. The three-body interactions are parametrized with Judd parameters, T^k, and the corresponding effective operators t_k ($k = 2$, 3, 4, 6, 7, and 8) which transform according to definite irreducible representations of G_2 and R_7 [29].

The standard, one-electron c.f. Hamiltonian H_{CF} is described by the product $B_q^k(i)C_q^k(i)$ with summation i over all electrons of the ion of interest [29]. B_q^k are the real c.f. parameters and C_q^k the spherical tensors of rank k equal to or less than six for the 4f elements. The values of k and q will be constrained by the point symmetry of the RE^{3+} site. For the $\mathrm{C}_{3\mathrm{v}}$ site symmetry, the c.f. Hamiltonian has the following form:

$$H_{\mathrm{CF}} = B_0^2 C_0^2 + B_0^4 C_0^4 + B_3^4(C_{-3}^4 - C_3^4) + B_0^6 C_0^6 + B_3^6(C_{-3}^6 - C_3^6) + B_6^6(C_{-6}^6 + C_6^6) \tag{2}$$

The best fit set of the c.f. parameters was obtained by the least-squares refinement through

minimizing the rms function σ between the observed and calculated energy level values [37].

As the starting values for the free ion parameters those for the LaF_3:RE^{3+} system [1] were utilized. The c.f. parameters from earlier calculations for the other REOF:RE^{3+} systems [20–24] were employed as the *a priori* values, too. The method used varies simultaneously both the free ion and c.f. parameters using a non-truncated set of wave functions. Calculations involve a diagonalization of two square matrices of sizes 666 and 670 [38]. As the literature survey indicated, the two requirements for a complete simulation, i.e. the use of a complete set of the basis functions and the simultaneous treatment of the free ion and c.f. effects, were fulfilled in this work for the first time.

3.3.2. Analysis of experimental data. The energy level scheme of the Dy^{3+} ion was resolved according to the group theoretical rules for the C_{3v} site symmetry. 153 Stark levels out of 1001 levels were derived from the absorption and luminescence spectra. A set of 20 parameters including 14 free ion and six c.f. parameters was used in the final simulation of the energy level scheme. The degrees of freedom are high enough to allow a reliable variation of all parameters involved.

In the beginning of the simulation only the Racah parameter E_0 and the spin–orbit coupling constant ζ_{4f} together with the c.f. parameters were refined by using the c.f. components of the two lowest terms ^{6}H and ^{6}F. After achieving constant values of the c.f. parameters more energy levels and additional free ion parameters such as the other Racah parameters, E_1, E_2, and E_3, and those of Trees, α, β, and γ, were included into the simulations. The Judd parameters were the last ones incorporated. However, the parameters T^3 and T^4 were left with fixed values after a few iteration cycles because they assumed unstable values.

The energy level scheme of the Dy^{3+} ion was well simulated as a whole. A good agreement between the observed and calculated level values was achieved with the rms deviation of 17 cm^{-1}. The isolated ^{6}H and ^{6}F terms of the Dy^{3+} ion are well separated from the higher excited terms and can be treated as a separate system which gives a very good fit. The inclusion of the higher excited levels with increasing mixing of the J multiplets changes the best fit B_q^k sets and impairs somewhat the overall simulation. The model involving the adjustment of both the free ion and c.f. parameters usually gives a good fit. Certain 'anomalous' multiplets which remain badly fitted, such as $^1D_2$ of Pr^{3+} [39], $^2H2_{11/2}$ of Nd^{3+} [40], or $^3K_8$ of Ho^{3+} [41], are found when the one-electron c.f. parameters are optimized alone [46]. In the case of DyOF no anomalous simulation was obtained for any individual state.

3.3.3. Free ion parametrization. The calculated free ion parameters (table 2) are similar to those obtained for LaF_3:RE^{3+} [1] or $LaCl_3$:RE^{3+} [4]. This was to be expected since the energies of the centres of the gravity of the c.f. multiplets, i.e. the $^{2S+1}L_J$ states, do not vary much from one host lattice to another [31]. In contrast, the Racah parameters E_0, E_1, E_2, and E_3, and the spin–orbit coupling constant ζ_{4f} (23 429, 4689, 23.17, 478, and 870 cm^{-1} for Nd^{3+} [21] and 46 314, 5204, 25.46, 518, and 1150 cm^{-1} for Sm^{3+} [22]) increase with increasing number of 4f electrons in the REOF series. The interconfigurational terms, i.e. the Trees and Judd parameters, show no clear trends. The parameters are well defined with low estimated standard deviations indicating the high quality of the simulation.

Table 2. The phenomenological free ion and c.f. parameters with estimated standard deviation. The calculated c.f. parameters were obtained by a modified point charge model.

Parameter	Exp. (cm^{-1})	Calc. (cm^{-1})
E_0	55 299(1)	
E_1	6171.9(2)	
E_2	30.40(1)	
E_3	623.84(5)	
α	18.11(2)	
β	−603(2)	
γ	1600(1)	
T^2	350(1)	
T^3	[78]	
T^4	[41]	
T^6	−360(11)	
T^7	350(8)	
T^8	345(6)	
ζ_{4f}	1915(1)	
B_0^2	57(16)	−870
B_0^4	1717(31)	1831
B_0^4/B_3^4	−1.350	−1.167
B_3^4	−1272(21)	−1569
B_0^6	1204(35)	957
B_0^6/B_3^6	2.165	1.018
B_3^6	556(31)	940
B_0^6/B_6^6	1.881	0.865
B_0^6	640(31)	1106
No of levels	153/1001	
σ	17	

3.3.4. Crystal field parametrization. The present simulation can be considered good with a low rms deviation and the absence of large individual discrepancies between the calculated and experimental data. The B_0^2 value was found to be close to zero whereas the fourth- and sixth-rank parameters assumed high values (table 2) which are approximately restricted to the ratios allowed for the ideal cubic symmetry, i.e. $B_0^4/B_3^4 = -0.837$, $B_0^6/B_3^6 = 1.656$, and $B_0^6/B_6^6 = 1.579$ [43]. These results indicate only a slight distortion from cubic structure.

The set of parameters is consistent with those for the REOF:RE^{3+} cases studied so far (table 3) [20–24]. It is expected that the c.f. effect should decrease as a function of increasing number of 4f electrons due to the increasing nuclear charge. However, only the Nd^{3+}, Sm^{3+}, and Dy^{3+} ions are in their 'natural' environment and for the Eu^{3+} and Tb^{3+} ions only the ground term ^7F_J has been employed in the simulation [23, 24]. These facts may affect the comparison. The expected evolution was observed from Pr^{3+} to Tb^{3+}, but beyond Tb^{3+} the c.f. effect seems to get stronger again. This can most easily be seen from the evolution of the c.f. strength parameter S (table 3) which is a quantitative measure of the strength of the c.f. interaction in a particular host [7]:

$$S = \left\{ \frac{1}{3} \sum_k \frac{1}{2k+1} \left[(B_0^k)^2 + 2 \sum_{q>0} ((B_q^k)^2 + (S_q^k)^2) \right] \right\}^{1/2} \tag{3}$$

where B_q^k and S_q^k are the real and imaginary c.f. parameters.

The influence of the nuclear charge beyond Tb^{3+} may be cancelled by two effects.

Table 3. The evolution of the free ion and B_q^k parameters in the REOF series. The data were obtained for Pr^{3+}, Nd^{3+}, Sm^{3+}, Eu^{3+}, Tb^{3+}, and Dy^{3+} in YOF [20], NdOF [21], SmOF [22], LaOF [23], LaOF [24], and DyOF (this work) matrices, respectively. All values are in cm^{-1} units.

Parameter	YOF:Pr^{3+}	NdOF	SmOF	LaOF:Eu^{3+}	LaOF:Tb^{3+}	DyOF
B_0^2	−124	−144	−200	−28	−36	57
B_0^4	1612	1839	1786	1162	1344	1717
B_0^4/B_3^4 [a]	−0.71	−1.12	−1.35	−0.86	−1.06	−1.35
B_3^4	−2276	−1643	−1308	−1347	−1272	−1272
B_0^6	1237	1005	1139	866	835	1204
B_0^6/B_3^6 [a]	1.13	1.16	1.54	1.8	2.0	2.16
B_3^6	1096	866	739	482	418	556
B_0^6/B_6^6 [a]	1.31	1.24	1.41	1.242	2.34	1.88
B_6^6	745	812	810	697	357	640
S	780	650	583	490	469	543
No of levels	58/91	122/182[b]	195/1001[b]	21/49	19/49	153/1001[b]
σ	15	17	17	10	5	17

[a] Ideal cubic ratios: $B_0^4/B_3^4 = -0.837$, $B_0^6/B_3^6 = 1.656$, and $B_0^6/B_6^6 = 1.579$ [43].
[b] Kramers doublets.

Firstly, it was observed that the values of the A_q^4 lattice sum parameters given by equation (4) (next section) remain nearly constant throughout the whole REOF series. In contrast, the A_q^6 parameters increase significantly (∼20%) with decreasing ionic radius from the Pr^{3+} to the Dy^{3+} ion. The $\langle r^k \rangle$ free ion radial integrals drastically decrease from Pr^{3+} to the middle of the RE^{3+} series but then smoothen out [47]. The evolution of the lattice sum parameters and radial integrals may be the reason for the increase in the c.f. effect beyond Tb^{3+}. Secondly, the higher (5s and 5d) orbitals introduce different parity contributions to the 4f configuration which strengthens the c.f. effect. This effect is expected to become important for the heavier rare earths due to the lanthanide contraction. At the moment, no further conclusions can be drawn because of the lack of information about the effective interactions and the energy separation between the different configurations.

The contributions from the orbitally [44] and/or spin [45] correlated two-electron c.f. interactions may have to be taken into account in the calculations, too. From a theoretical point of view, the additional parameters may give some advantages, but, in practice, their large number requires the use of simplifications and rejection of the less important parameters [46]. The decision to include additional parameters may prove to be rather complicated if the choice is based on the rather inaccurate experimental data. Some success—such as the correct simulation of the $^2H2_{11/2}$ level splitting for the Nd^{3+} ion [42]—has been achieved by including the two-electron c.f. interaction.

3.4. Electrostatic point charge model calculations

The c.f. Hamiltonian is expressed as a sum of products of the Racah tensor operators, C_q^k, and the c.f. parameters, B_q^k (2). According to the modified electrostatic point charge model (PCEM), the c.f. parameters can also be given as follows:

$$B_q^k = \tau^{-k}(1 - \sigma_k)A_q^k\langle r^k \rangle \tag{4}$$

where $\langle r^k \rangle$ are the free ion radial integrals and A_q^k the lattice sum parameters. The correction factors σ_k describe the shielding effect of the 6s, 5d, and 5p electrons. The expansion factor τ

describes the expansion of the 4f wave functions in the solid state when compared to the free ion. The expansion factor and the shielding factor σ_2 were calculated as follows [47]: $\tau = 0.767 - (0.00896N) = 0.6807$ and $\sigma_2 = 0.6902 - (0.0121N) = 0.580$ where N is the number of 4f electrons, nine for the Dy^{3+} ion. The σ_4 and σ_6 values were assumed as constants across the RE series [47]. The free ion radial integrals $\langle r^k \rangle$ for the Dy^{3+} ion, $\langle r^2 \rangle = 0.7814$, $\langle r^4 \rangle = 1.505$, and $\langle r^6 \rangle = 6.148$, have been calculated by the Dirac–Fock method [48].

The electrostatic lattice sum parameters A_q^k were calculated according to the following formula [49]:

$$A_q^k = e^2 \left[\frac{(k+q)!}{(k-q)!} \right] \sum_j \frac{g_j}{\rho_j^{k+1}} \frac{(1-x_j^2)^{-q/2}}{2^k k!} \frac{d^{k-q}(x_j^2-1)^2}{dx_j^{k-q}} \exp(-iq\beta_j) \qquad (5)$$

where the sum j runs over the point charges with a charge g_j in the selected lattice space. α_j, β_j and ρ_j are the polar coordinates of the point charge and x_j is $\cos\alpha_j$.

The structural information for calculations was taken from the results of the Rietveld profile analysis carried out with our XRD data. The effective charge for Dy^{3+} ($g_{Dy} = +1.80$) was optimized in a way described earlier [23] and is close to the value found for the Y^{3+} ion in Y_2O_3 ($g_Y = +1.6$–1.7) [50].

The shielding factors σ_k are dependent on k but they have only a minor effect on the B_q^4 and B_q^6 parameter values whereas the B_0^2 parameter is influenced to a much greater extent. The effect of the expansion factor τ is the opposite. As a whole, the free ion radial integrals $\langle r^k \rangle$ ($k = 2, 4, 6$) are modified by a factor of 0.8, 3.5, and 8, respectively, when both the shielding and expansion corrections have been applied.

The point-charge calculations (table 2) yielded c.f. parameters of rank four (B_0^4 and B_3^4) and B_0^6 close to the values obtained experimentally, whereas the B_0^2, B_3^6, and B_6^6 values were found to be too large. The calculated B_0^2 value is too large probably due to the purely ionic model which does not take into account covalence effects. The calculated B_0^4/B_3^4 ratio is closer to the ideal cubic value than the experimental ratio. The calculated sixth-rank parameter ratios are smaller whereas the experimental ones are larger than the ideal ratios (table 3). As a whole, the fourth- and sixth-rank parameters were estimated rather well taking into account the simple model.

3.5. Paramagnetic susceptibility of DyOF

The temperature dependence of the reciprocal magnetic susceptibility (χ^{-1}) of the powder sample of DyOF (figure 4) follows the Curie–Weiss law ($\chi = 14.06/(T + 9.2)$) between 10 and 360 K. The calculated magnetic moment is $10.57\mu_B$, which agrees well with the expected value, $10.63\mu_B$, for the free ion ground term $^4I_{9/2}$ of the Dy^{3+} ion. Below 10 K the experimental data exhibit a deviation from the Curie–Weiss law and the reciprocal susceptibility shows a clear minimum at 3.6 K (figure 4). The minimum can be attributed to a three-dimensional antiferromagnetic ordering in the Dy^{3+} sublattice. It is not known whether structural modifications were associated with the antiferromagnetic ordering. The observed Néel temperature of 3.6 K for DyOF is considerably higher than the value reported for Dy_2O_3 [51] but identical to those obtained for $DyVO_4$ [52] and $DyPO_4$ [53]. In the case of SmOF, isostructural to DyOF, no magnetic ordering has been reported down to 1.5 K [54].

The analysis of the structure of DyOF can be used to explain the magnetic interactions. Dy^{3+} is eight coordinated to four oxygens and four fluorides (see the section on crystal structure) and thus four different Dy–O(F)–Dy superexchange pathways are operative. Since

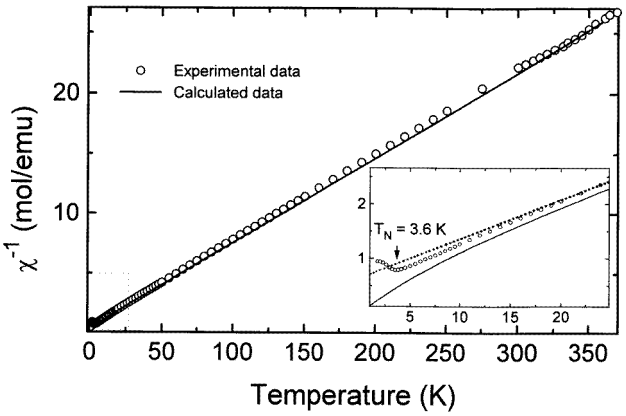

Figure 4. Experimental (circles) and calculated (solid line) paramagnetic susceptibility of DyOF at temperatures between 1.7 and 370 K. The values calculated by the Curie–Weiss law ($\chi = 14.06/(T + 9.2)$) are given with a dotted line.

the Dy–O distances are shorter than the Dy–F ones, it is expected that the superexchange should be more effective in the former pathway where oxygen is involved. However, due to the important deviation of the Dy–O(F)–Dy angles (102–116°) from the optimum superexchange angle (180°) and the shielded position of the 4f orbitals, a value of the Néel temperature as small as 3.6 K can be anticipated.

The temperature dependence of the experimental paramagnetic susceptibility was compared with the calculated values obtained from the van Vleck formula [55]:

$$\chi = N_A\beta^2 \sum_i \left(\frac{\langle \Phi_i|\mu|\Phi_i\rangle^2}{kT} - 2\sum_{i\neq j} \frac{\langle \Phi_i|\mu|\Phi_j\rangle\langle \Phi_j|\mu|\Phi_i\rangle}{E_i - E_j} \right) B_i \qquad (6)$$

where $B_i = \exp(-E_i/kT)/\sum_i d_i \exp(E_i/kT)$ and $\mu = \bar{h}(L + 2S)$.

The first-order matrix elements, $\langle \Phi_i|\mu|\Phi_i\rangle$, lead to the Curie behaviour and the second-order ones, $\langle \Phi_i|\mu|\Phi_j\rangle\langle \Phi_j|\mu|\Phi_i\rangle$, to the temperature-independent susceptibility. N_A and β are the Avogadro constant and the Bohr magneton, respectively. The wave functions Φ_i and Φ_j are the eigenfunctions of the Hamiltonian corresponding to the eigenvalues E_i and E_j of the energy levels for the Dy^{3+} ion. μ is the magnetic operator, B_i is the thermal population of the energy levels according to the Boltzmann distribution law, and d_i is the degeneracy of the energy level.

The calculation was carried out by using the wave functions obtained from the energy level simulation. The levels up to 10 000 cm^{-1} were accounted for in the calculation together with J mixing of the levels. The calculated parallel ($\chi_\parallel$) and perpendicular ($\chi_\perp$) susceptibilities show large anisotropy at low temperatures below 50 K. Good agreement between the observed and calculated susceptibility was observed above the Néel temperature (figure 4). The results indicate that the wave functions and the whole energy level simulation were correct. Moreover, the inclusion of the higher excited levels—having only negligible contribution—has not impaired the simulation of the magnetic susceptibility.

4. Conclusions

The optical absorption and emission spectra of the Dy^{3+} ion in the hexagonal DyOF and GdOF, respectively, were measured at selected temperatures down to 9 K. The analysis of the spectra yielded 153 c.f. components representing 39 *SLJ* states. The analysis of the polarization and the intensity of the lines may have modified the assignments of the transitions but the former investigations could not be carried out due to the lack of single-crystal samples. However, as a whole, the results of the c.f. analysis can be considered reliable. The energy level scheme was successfully simulated according to the C_{3v} site symmetry by a phenomenological model using 14 free ion and six c.f. parameters resulting in an rms deviation of 17 cm^{-1}.

The free ion parameters resemble to those observed for Dy^{3+} in other RE^{3+} systems. The increase in the free ion parameter values from Nd^{3+} to Sm^{3+} and from Sm^{3+} to Dy^{3+} indicates increasing electrostatic repulsion and spin–orbit coupling between the 4f electrons. The B_0^2 value close to zero and the c.f. parameter ratios B_0^4/B_3^4 and B_0^6/B_q^6 ($q = 3$ and 6) close to the ideal cubic values reflect the cubic pseudosymmetry of the REOF structure. Similar results were obtained for the c.f. parameters calculated by the modified electrostatic point charge model which used the XRD structure data obtained by the Rietveld refinement method.

The present results were found to be consistent with those from the previous studies concerning Pr^{3+}, Nd^{3+}, Sm^{3+}, Eu^{3+}, and Tb^{3+}. In the entire REOF:RE^{3+} series, the phenomenological c.f. parameters decrease from Pr^{3+} to Tb^{3+}. Further work is currently in progress with the heavier RE^{3+} ions (from Ho^{3+} to Yb^{3+}) in the RE oxyfluoride host.

The measured magnetic susceptibility from 1.7 to 360 K follows paramagnetic behaviour close to the Néel temperature, 3.6 K, below which DyOF is ordered antiferromagnetically. The low Néel temperature can be explained by weak superexchange in the Dy^{3+} sublattice. By using the experimentally determined free ion and c.f. wave functions, the theoretical paramagnetic susceptibility was calculated and good agreement was found between the calculated and observed susceptibilities down to the Néel temperature.

Acknowledgments

Financial support from the Academy of Finland (project No 4966) to EK and JH is gratefully acknowledged. The authors are also indebted to Professor Jussi Valkonen (University of Jyväskylä) for the use of the XRD equipment.

References

[1] Carnall W T, Goodman G L, Rajnak K and Rana R S 1989 *J. Chem. Phys.* **90** 3443
[2] Goodman G L, Carnall W T, Rana R S, Vandevelde P, Fluyt L and Görller-Walrand C 1986 *J. Less-Common Met.* **126** 283
[3] Morrison C A and Leavitt R P 1979 *J. Chem. Phys.* **71** 2366
[4] Jayasankar C K, Richardson F S and Reid M F 1989 *J. Less-Common Met.* **148** 289
[5] Rana R S, Shertzer J, Kaseta F W, Garvey R, Rana D and Feng S Y 1988 *J. Chem. Phys.* **88** 2242
[6] Gruber J B, Leavitt R P, Morrison C A and Chang N C 1985 *J. Chem. Phys.* **82** 5373
[7] Chang N C, Gruber J B, Leavitt R P and Morrison C A 1982 *J. Chem. Phys.* **76** 3877
[8] Karayianis N, Wortman D E and Morrison C A 1976 *Solid State Commun.* **18** 1299
[9] Wardzynska M and Wanklyn B M 1977 *Phys. Status Solidi* b **40** 663
[10] Reid M F and Richardson F S 1985 *J. Chem. Phys.* **83** 3831
[11] Davydova M P, Zdanovich S B, Kazakov B N, Korableva S L and Stolov A L 1977 *Opt. Spectrosc.* **42** 327
[12] Wortman D E and Sanders D 1971 *J. Chem. Phys.* **55** 3212

[13] Pillai S M and Vallabhan C P G 1986 *Phys. Status Solidi* b **134** 383
[14] Veyssie M and Dreyfus B 1967 *J. Phys. Chem. Solids* **28** 499
[15] Hölsä J and Kestilä E 1995 *J. Alloys Compounds* **225** 89
[16] Caro P E 1968 *J. Less-Common Met.* **16** 367
[17] Mann A W and Bevan D J M 1970 *Acta Crystallogr.* B **26** 2129
[18] Taoudi A, Laval J-P and Frit B 1994 *Mater. Res. Bull.* **29** 1137
[19] Laval J-P, Abaouz A, Frit B, Roult G and Harrison W T A 1988 *Eur. J. Solid State Inorg. Chem.* **25** 425
[20] Antic-Fidancev E, Hölsä J, Krupa J-C, Lemaitre-Blaise M and Porcher P 1992 *Proc. 4th Int. Conf. on Solid State Chemistry (Dresden, 1992)* (Frankfurt/Main: Gesellschaft Deutscher Chemiker) p 157
[21] Antic-Fidancev E, Hölsä J, Kestilä E, Lemaitre-Blaise M, Porcher P and Ylhä P 1995 unpublished results
[22] Hölsä J, Kestilä E and Porcher P 1995 unpublished results
[23] Hölsä J and Kestilä E 1995 *J. Chem. Soc. Faraday Trans.* **91** 1503
[24] Antic-Fidancev E, Hölsä J, Krupa J-C, Lemaitre-Blaise M and Porcher P 1993 *Int. Conf. on Luminescence (ICL'93) (Storrs, CT, 1993)* pp Th4-33
[25] Hölsä J and Niinistö L 1980 *Thermochim. Acta* **37** 155
[26] Boudreaux E A and Mulay L N 1976 *Theory and Applications of Molecular Paramagnetism* (New York: Wiley)
[27] Sakthivel A and Young R A 1991 *Program DBWS-9006PC for Rietveld Analysis of x-ray and Neutron Powder Diffraction Patterns* (Atlanta, GA: Georgia Institute of Technology)
[28] Henry N F M and Lonsdale K (eds) 1969 *International Tables Crystallography* vol 1 (Birmingham: Kynoch) p 273
[29] Wybourne B G 1965 *Spectroscopic Properties of Rare Earths* (New York: Interscience)
[30] Prather J L 1961 *US National Bureau of Standards Monograph* 19
[31] Hüfner S 1978 *Optical Spectra of Transparent Rare Earth Compounds* (New York: Academic) p 107
[32] Peacock R 1975 *Struct. Bond.* vol 22 (Berlin: Springer) p 83
[33] Hölsä J, Lamminmäki R-J and Porcher P 1995 unpublished results
[34] Imbusch G F 1992 *Optical Properties of Excited States in Solids (NATO ASI Series B: Physics **301**)* ed B Di Bartolo (New York: Plenum) p 207
[35] Hölsä J, Piriou B and Räsänen M 1993 *Spectrochim. Acta* A **49** 465
[36] Porcher P 1988 *Phase Transitions* **13** 233
[37] Antic-Fidancev E, Lemaitre-Blaise M, Porcher P and Hölsä J 1992 *Phys. Status Solidi* a **130** K147
[38] Porcher P 1989 *Computer Programs Reel and Image for the Simulation of d^N and f^N Configurations Involving the Real and Complex Crystal Field Parameters* (Meudon: CNRS)
[39] Garcia D and Faucher M 1989 *J. Chem. Phys.* **90** 5280
[40] Faucher M, Garcia D, Caro P, Derouet J and Porcher P 1989 *J. Physique* **50** 219
[41] Crosswhite H and Newman D J 1984 *J. Chem. Phys.* **81** 4959
[42] Rukmini E, Jayasankar C K and Reid M F 1994 *J. Phys.: Condens. Matter* **6** 5919
[43] Caro P 1976 *Structure Electronique des Elements de Transition* (Paris: PUF)
[44] Yeung Y Y and Newman D J 1987 *J. Chem. Phys.* **86** 6717
[45] Reid M F 1987 *J. Chem. Phys.* **87** 2875
[46] Faucher M and Moune O K 1994 *ICFE-2 (Helsinki, 1994) Book of Abstracts* 76
[47] Leavitt R P, Morrison C A and Wortman D E 1975 *Harry Diamond Laboratories Report* TR-1673
[48] Freeman A J and Desclaux J P 1979 *J. Magn. Magn. Mater.* **12** 11
[49] Porcher P 1987 *Program Somaille for Point Charge Lattice Sum Calculations* (Meudon: CNRS)
[50] Jollet F, Noguera C, Thormat N, Gautier M and Duraud P 1990 *Phys. Rev.* B **42** 7587
[51] 1970 *Landolt–Börnstein New Series* ed J B Goodenough and J M Longo (Berlin: Springer)
[52] Guo M-D, Aldred A T and Chan S-K 1987 *J. Phys. Chem. Solids* **48** 229
[53] Loong C-K, Soderholm L, Xue J S, Abraham M M and Boatner L A 1994 *J. Alloys Compounds* **207/208** 165
[54] Hölsä J, Kestilä E, Porcher P and Sáez-Puche R 1995 unpublished results
[55] van Vleck J H 1932 *The Theory of Electric and Magnetic Susceptibilities* (London: Oxford University Press)